ChoroidNET: A Dense Dilated U-Net Model for Choroid Layer and Vessel Segmentation in Optical Coherence Tomography Images

TIN TIN KHAING[1,2], TAKAYUKI OKAMOTO[1], CHEN YE[3], MD. ABDUL MANNAN[3], HIROTAKA YOKOUCHI[4], KAZUYA NAKANO[5], PAKINEE AIMMANEE[2], STANISLAV S. MAKHANOV[2], AND HIDEAKI HANEISHI[3]

[1]Graduate School of Science and Engineering, Chiba University
[2]School of ICT, Sirindhorn International Institute of Technology, Thammasat University
[3]Center for Frontier Medical Engineering, Chiba University
[4]Department of Ophthalmology and Visual Science, Graduate School of Medicine, Chiba University
[5]Institute for Tenure Track Promotion, University of Miyazaki

Corresponding author: Takayuki Okamoto (t_okamoto@chiba-u.jp).

ABSTRACT Understanding the changes in choroidal thickness and vasculature is important to monitor the development and progression of various ophthalmic diseases. Accurate segmentation of the choroid layer and choroidal vessels is critical to better analyze and understand the choroidal changes. In this study, we develop a dense dilated U-Net model (ChoroidNET) for segmenting the choroid layer and choroidal vessels in optical coherence tomography (OCT) images. The performance of ChoroidNET is evaluated using an OCT dataset that contains images with various retinal pathologies. Overall Dice coefficient of 95.1 ± 0.4 and 82.4 ± 2.4 were obtained for choroid layer and vessel segmentation, respectively. Comparisons show that among state-of-the-art models, ChoroidNET, which produces results that are consistent with ground truths, is the most robust segmentation framework.

INDEX TERMS Choroid Layer, Choroidal Vessels, ChoroidNET, Dense Dilated U-Net, Optical Coherence Tomography (OCT).

I. INTRODUCTION

In optical coherence tomography (OCT) images, the choroid is a dense vascular layer between the retina and the sclera. It comprises choroidal vessels (luminal area) embedded in elastic connective tissues (stromal area). Its main function is to supply oxygen and nourishment to the outer retina. The thickness and vascularity index of the choroid are choroidal biomarkers [1] that facilitate the diagnosis, prognosis, and treatment of various ophthalmic diseases or their pathological conditions such as age-related macular degeneration (AMD) [2], choroid neovascularization (CNV) which is a pathology that occurs in wet AMD [3], diabetic macular edema (DME) [4], and retinitis pigmentosa (RP) [5][6].

OCT is a non-invasive imaging technique that captures a cross-sectional view of the retina, including the choroid. With rapid development in optical imaging technology, enhanced depth imaging OCT (EDI-OCT) and swept-source OCT (SS-OCT) enable better visualization of the choroid than the conventional spectral-domain OCT (SD-OCT) [7][8]. Figure 1 shows an OCT image of the components in the choroid layer, i.e., the upper boundary of the choroid (blue dashed line), the lower boundary of the choroid (green dashed line), the choroidal vessels, and the stromal area.

The choroid has an inhomogeneous texture because it contains vessels. The contrast between the choroid and the sclera is usually low in an OCT image, and thus the lower boundary of the choroid, called the choroid-sclera interface (CSI), is fuzzy and difficult to distinguish from the choroid. The choroid layer and choroidal vessels in OCT images must thus be manually annotated, which is time-consuming, error-prone (due to indistinct vascular structures), and subject to interobserver variability. Although some automated segmentation approaches are available, individual applications are required for segmenting the choroid layer

and choroidal vessels. To the best of our knowledge, this study is the first to combine the segmentation of the choroid layer and vessels, which is clinically important. This is done using a deep learning model trained on eyes with various pathologies.
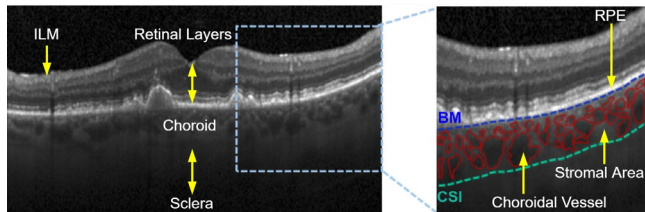

FIGURE 1. Choroid region in an OCT image (ILM – internal limiting membrane, RPE – retinal pigment epithelium, BM – Bruch's membrane, and CSI – choroid-sclera interface).

In this work, we propose a dense dilated U-Net model called ChoroidNET for segmenting the choroid layer and choroidal vessels in OCT images. The automatic extraction of these regions would greatly assist ophthalmologists in diagnosis and treatment monitoring. ChoroidNET uses the U-Net [9] as its backbone architecture and integrates dilated convolutions with different dilation factors at the bottleneck. The dense connection of dilated convolutions exploits image contexts at multiple scales and improves segmentation performance. The experimental results demonstrate that ChoroidNET significantly outperforms existing state-of-the-art methods. We perform ablation studies to confirm the performance of ChoroidNET. Our ultimate goal is to automatically quantify clinical parameters that can be derived from the choroid, such as the luminal-to-stromal ratio and choroidal thickness.

The main contributions of this work are:

1) development of ChoroidNET for segmenting the choroid layer and choroidal vessels;
2) highlighting of the use of dilated convolutions in both layer and vessel segmentation;
3) robust segmentation of OCT images of eyes with various retinal pathologies;
4) qualitative and quantitative evaluation using manually annotated ground truths to determine the reproducibility of ChoroidNET.

II. LITERATURES

Many traditional image processing methods have been proposed for segmenting the choroid layer fully or semi-automatically for various retinal diseases. Graph search algorithm [10], graph cuts and dynamic programming [11, 12], min-cut max-flow graph theory [13], the Dijkstra shortest path algorithm [14-16], active contour [17], and the level set method [18] have been applied to detect the choroid boundaries in OCT images. Poor robustness is the main drawback of choroid segmentation techniques based on traditional image processing since they are highly sensitive to severe pathological images.

Deep learning has gained increasing interest in medical image processing research. Several deep learning models were recently applied to choroid segmentation to improve performance. To detect the choroid boundaries, Sui et al. [19] presented a multi-scale convolutional neural network (CNN) to learn the edge weights in a graph searching approach. Masood et al. [20] performed automatic choroid segmentation using a patch-based CNN and morphological operations. A variety of deep learning models such as CNN, residual network, recurrent neural network, and squeeze and excitation network were explored in the choroid segmentation works of Kugelman et al. [21] and Alonso-Caneiro et al. [22]. They investigated the effects of patch size and the network architectures, and image pre-processing techniques on their patch-based and semantic segmentation networks. Chen et al. [23] used two SegNet models [24] to generate edge probability maps for BM and the CSI. Then, seam carving was applied to obtain a full choroid layer by finding a path of connected pixels between BM and the CSI. Devalla et al. [25] presented the dilated-residual U-Net model (DRUNET) for segmenting optic nerve head tissues, which contain the choroid, in OCT images of glaucomatous and healthy eyes. Zhang et al. [26] infused a biomarker prior into a global-to-local network (BIONET) for choroid segmentation. BIONET is composed of 1) a biomarker infused prediction network that learns the biomarker features, 2) a global multi-layered segmentation module that initially segments all layers (retinal layers and the choroid layer) in OCT images, and 3) a local choroid segmentation module that segments the choroid using the result from the global module and the learned biomarker features. Hsia et al. [27] segmented the choroid layer using a mask region-based CNN model, composed of deep residual network and feature pyramid networks. The choroid segmentation performance of deep learning models is very competitive and generally better than those of traditional image processing techniques.

Algorithms based on traditional image processing techniques have been developed for choroidal vessel segmentation. Srinath et al. [28] initially defined the RPE by finding the brightest region and the CSI by calculating the structural similarity index between the choroid and the sclera. Then, choroidal vessels were segmented in the region between the RPE and the CSI using the level set method.

Recently, Liu et al. [29] presented a deep-learning-based choroidal vessel segmentation model adapted from RefineNet [30]. There have been attempts to obtain the choroidal thickness and vasculature from SS-OCT images. Zheng et al. [31] detected the choroid's upper and lower boundaries in OCT images using the Residual U-Net model [32] and then performed binarization to detect the choroidal vessels using Niblack's algorithm. Zhou et al. [33] applied an attenuation correction approach to compensate for the attenuated light in SS-OCT images as a pre-processing step in choroid segmentation. Then, choroidal vessel maps, which enable the choroidal vasculature to be visualized without

OCT angiography, were generated using a projection of OCT structural information.

A summary of performances, datasets, advantages, and drawbacks/limitations of some existing choroid layer and vessel segmentation methods, are discussed in Table 1.

III. METHODS

This section describes the network architecture and components of ChoroidNET. ChoroidNET is a patch-based model that adopts the structure of U-Net [9]. To denoise and enhance the contrast of OCT images, we preprocess each extracted patch using normalized gamma-corrected contrast-limited adaptive histogram equalization [34]. Training is then performed using the preprocessed patches. During training, we also perform data augmentation, which includes affine transformation, horizontal flipping, random distortion, and zooming.

A. NETWORK ARCHITECTURE

Figure 2 shows the network architecture of ChoroidNET. The model comprises a layer segmentation module (LSM) and a vessel segmentation module (VSM). Each module consists of an encoder path, a decoder path, and a dilation block, which uses dense dilated convolutions, instead of standard convolutions. The blocks used in the network are defined as follows. A standard (purple) block corresponds to the resulting activation map from two consecutive 3×3 standard convolutions. All layers in a standard block are regularized by DropBlock (DB) [35], batch-normalized (BN) [36], and activated by a rectified linear unit (ReLU) [37]. A gray block represents the activation map forwarded from the encoder path that is concatenated with the corresponding up-sampled map in the decoder path. The red and yellow blocks, at the bottleneck of LSM and VSM, respectively, are dilation blocks that comprise six dilated convolutions with different dilation factors. These dilation blocks help ChoroidNET to overcome the loss of detailed spatial information and difficulty in extracting contextual semantic features. ChoroidNET thus has a good segmentation accuracy, resulting in smooth boundaries of the choroid layer. The intersection area of the input patch and the choroid layer prediction from LSM is fed into VSM to obtain a more consistent segmentation of choroidal vessels.

Encoder Path. At each level of the encoder path, the number of feature vectors is doubled. Thus, the bottommost level of the encoder path generates high-level semantic features. The purpose of the encoder path is to capture the contextual information of the input patches. This information is then fed to the decoder path through skip connections [38].

Decoder Path. After each level of the decoder path, a 2×2 up-sampling operation is applied to restore the image to its original size. The purpose of the decoder path is to perform semantic segmentation by concatenating up-sampled outputs and the contextual information transferred from the encoder path via skip connections. The features generated by the dilation block are added to achieve multi-scale context aggregation. Finally, a 1×1 convolution and a sigmoid activation are applied to obtain the pixel-wise binary segmentation for each pixel.

Dilated Convolutions. A dilated convolution refers to a convolution conducted with a dilated filter. Yu et al. [39] and Chen et al. [40] reported that dilated convolutions can be used instead of down-sampling operations to expand the receptive field without degrading the resolution of intermediate feature maps by inserting zeros between the pixels of the kernel. Consider convolutional kernel K_l with a kernel size of $k \times k$ in dilated layer l. The receptive field F_{K_l} of kernel K_l can be calculated as:

$$F_{K_l} = k + (k-1) \times (D_{K_l} - 1) \qquad (1)$$

where D_{K_l} denotes the dilation rate of kernel K_l. Figure 3 shows how the dilated convolutions adaptively enlarge the field of views by increasing the dilation rates.

For the dilation block of LSM, we increase the dilation factors in increments of 2. We experimentally found that this increasing order of dilation factors yields better performance in the choroid layer segmentation. However, aggressively increasing dilation factors is less effective for small objects such as choroidal vessels. Dilated convolutions with increasing dilation factors lead to weak spatial inconsistency between neighboring pixels; thus, it fails to aggregate local features. To address this, Hamaguchi et al. [41] used a local feature extractor after large contexts are aggregated by increasing the dilation factors. The local feature extractor helps to extract local features by decreasing the dilation factors. Inspired by this concept, for the dilation block of VSM, we first increase the dilation factors gradually and then decrease them to recover consistency between neighboring pixels.

DropBlock. Dropout [42] is a widely used regularization technique for fully connected networks. It prevents the overfitting caused by coadaptation on the training dataset by reducing the complexity of the network architecture and randomly dropping out independent features. However, this technique is less effective for convolutional networks where the features are spatially correlated because semantic information can still leak through in the networks. Thus, Ghiasi et al. [43] proposed DropBlock [35], which is a form of structured dropout, for effectively regularizing convolutional networks. We apply DropBlock to prevent our network from overfitting and to effectively remove semantic information. Figure 4 shows how DropBlock discards some contiguous regions that contain certain semantic information from a feature map of the choroid layer.

TABLE 1. A brief description of recent existing methods for the choroid layer and vessel segmentation.

Authors	Segmentation Method		Dataset	Performance Metrics	Value	Advantages	Drawbacks/Limitations
	Layer	Vessel					
Chen et al. [13] (2015)	Detected the choroid upper boundary by thresholding and CSI by searching the shortest path of the graph with the max-min flow in the gradual intensity distance image.	-	212 peripapillary High Definition-OCT images of eyes from patients (disease unspecified)	Overlap ratio (Choroid Layer)	85.0%	Performance was evaluated in terms of inter- and intra-observer variability.	Thresholding-based upper boundary detection may be sensitive to severe pathology present in the image.
Hussian et al. [15] (2018)	Segmented the choroid layer using Dijkstra's short path algorithm and depth-based intensity normalization technique.	Segmented the choroidal vessels using Otsu's clustering method.	190 foveal-centered EDI-OCT images of eyes without a history of retinal diseases	Dice coefficient (Choroid Layer)	92.9%	Performance was validated against two expert observers.	To confirm the robustness, only two SS-OCT images of eyes with AMD and CNV were tested. Vessel segmentation performance was not reported.
Salafian et al. [16] (2018)	Transformed the input image into a neutrosophic space that contains true, false, and indeterminate sets. Then, the Dijkstra shortest path algorithm was applied to detect the choroid boundaries based on the calculated weights between pairs of nodes in the image.	-	15 foveal-centered and 17 peripapillary EDI-OCT images of healthy eyes and eyes with multiple sclerosis	Unsigned error (foveal-centered); Unsigned error (peripapillary)	3.34 pixels; 6.65 pixels	Choroid segmentation was performed in both peripapillary and foveal-centered OCT images.	The algorithm was tested on small datasets.
Lu et al. [17] (2013)	Segmented the choroid upper boundary using a variational active-contour model and CSI by minimizing an energy function model using a dynamic programming technique.	-	30 foveal-centered EDI-OCT images of eyes from patients with diabetes	Dice coefficient (Choroid Layer)	92.7 ± 3.6	Real-time human interaction was offered to guide CSI segmentation intelligently.	The algorithm may not be robust for the images which have poorer quality than EDI-OCT images.
Wang et al. [18] (2017)	Segmented the choroid layer using the level set method in which a distance regularization term, an edge constraint term, and a region (around the CSI) term are embedded to detect the indistinct CSI and to compensate for inconsistent textures in the choroid.	-	600 foveal-centered SS-OCT images from healthy subjects	(Choroid Layer) Dice coefficient; Mean signed difference; Mean unsigned difference	90.0 ± 4.0; 1.59 ± 1.65; 2.17 ± 1.77	Construction of a thickness map of the choroid layer in the same volume image was performed.	There is a lack of performance testing on pathological images.
Sui et al. [19] (2017)	Segmented BM and CSI using a convolutional neural network (CNN) which generates graph-edge weights for BM and CSI, and a graph searching technique.	-	912 foveal-centered EDI-OCT images (618 normal images and 294 macular edema images)	Mean square error (BM); Mean square error (CSI); Absolute error (BM); Absolute error (CSI)	0.9; 9.5; 4.6 ± 4.8; 11.4 ± 11.0	The multi-scale CNN combines local and global information, at coarse, middle, and fine image scales, which is important for object segmentation.	Choroidal vessel segmentation was not performed.
Masood et al. [20] (2019)	Segmented the choroid layer using a patch-based CNN model and morphological operations.	-	525 foveal-centered OCT images of healthy, short-sighted, glaucomatous, and DME eyes	Dice coefficient (Choroid Layer)	97.4 ± 2.3	High segmentation performance was claimed and the thickness map construction of the choroid layer in the same volume image was provided.	Choroidal vessel segmentation was not performed.

TABLE 1. (Continued)

| Authors	Segmentation Method		Dataset	Performance		Advantages	Drawbacks/Limitations
	Layer	Vessel		Metrics	Value		
Kugelman et al. [21] (2019)	Segmented the boundaries of the outer RPE and CSI using different deep learning methods such as standard U-Net, residual network, recurrent neural network, squeeze and excitation network, and the combined network, followed by a graph search procedure.	-	594 foveal-centered SD-OCT images of eyes from 99 healthy children	Mean absolute error (Outer RPE) / Mean absolute error (CSI)	0.44 ± 0.11 (in pixel) / 2.53 ± 1.52 (in pixel)	ILM segmentation was also included in their experiment. Comparisons of segmentation performance based on different patch sizes were also presented.	There is a lack of performance testing on pathological images.
Chen et al. [23] (2017)	Segmented BM and CSI using two SegNet models [24]. Then, the region between BM and CSI was filled to provide a full choroid layer segmentation.	-	62 foveal-centered EDI-OCT images of eyes with dry and wet AMD	Dice coefficient (Choroid Layer)	83.0 ± 0.1	The segmentation model is robust to the pathology in eyes with AMD.	Choroidal vessel segmentation was not performed.
Devalla et al. [25] (2018)	Segmented optic nerve head (ONH) tissues, including the choroid, using a dilated-residual U-Net model (DRUNET).	-	100 ONH-centered EDI-OCT images (40 healthy subjects and 60 subjects with glaucoma)	(Choroid Layer) Dice coefficient - healthy - glaucoma	90.6 ± 3.5 / 91.2 ± 5.0	Segmentation of other ONH tissues (lamina cribrosa, sclera, etc.) was included.	Choroidal vessel segmentation was not performed.
Zhang et al. [26] (2020)	Segmented the choroid layer using a biomarker-infused global-to-local network (Bio-Net).	-	1,280 foveal-centered OCT images of healthy eyes and eyes with CNV	(Choroid Layer) Dice coefficient - healthy - CNV	92.7 ± 0.0 / 90.2 ± 0.9	Visualization of choroidal vasculature in en-face images was further performed using a generative adversarial inpainting network.	Choroidal vessel segmentation in OCT images was not included.
Hsia et al. [27] (2021)	Segmented the choroid layer using a mask region-based CNN model, composed of ResNet and feature pyramid networks.	-	750 foveal-centered EDI-OCT images of healthy eyes	Accuracy (Choroid Layer)	87.5%	The performances of ResNet-50, ResNet-101, (ResNet-50 ∩ ResNet-101), and (ResNet-50 ∪ ResNet-101) were reported.	There is a lack of performance testing on pathological images. Choroidal vessel segmentation was not performed.
Srinath et al. [28] (2014)	Detected the choroid boundaries using structural similarity and adaptive Hessian technique.	Segmented the choroidal vessels using the level set approach.	OCT images	-	-	-	The algorithm may be sensitive to the retinal pathology.
Liu et al. [29] (2019)	-	Segmented the choroidal vessels using RefineNet [30].	40 foveal-centered SS-OCT images of eyes with emmetropes and high myopia.	Segmentation agreement C1 vs RefineNet C2 vs RefineNet	84.0 ± 3.5 / 82.3 ± 2.7	Good segmentation agreement between the RefineNet results and clinicians (C1 and C2) was achieved.	Choroid layer segmentation was not performed.
Zheng et al. [31] (2021)	Segmented the choroid's upper and lower boundaries using Residual U-Net [32].	Segmented the choroidal vessels using Niblack's binarization algorithm.	217 foveal-centered SS-OCT images of eyes without retinal pathology.	Failure ratio (2%) (Upper boundary) / Failure ratio (2%) (Lower boundary)	0.22 / 13.23	Six choroidal parameters were measured based on the choroid layer and vessel segmentation results.	The performance of choroidal vessel segmentation was not reported.

5
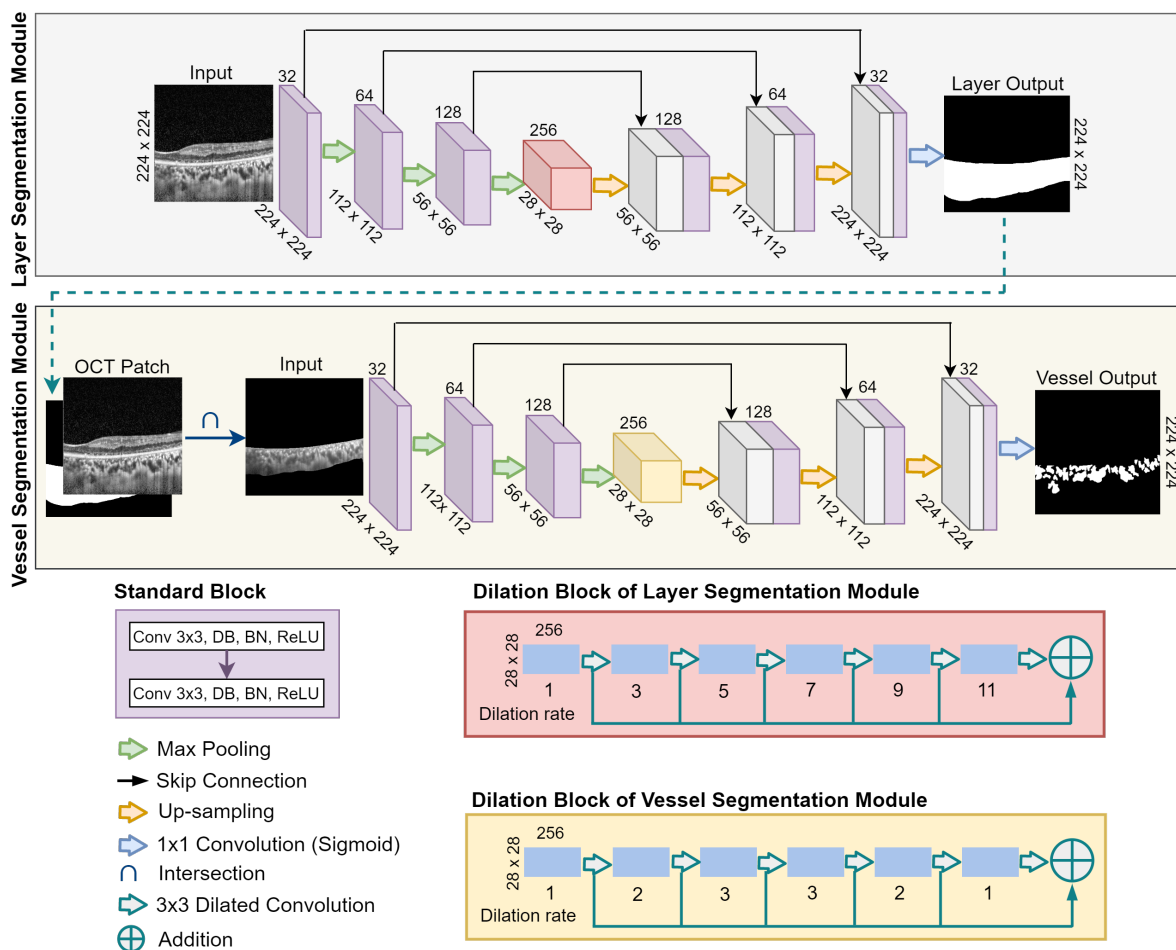
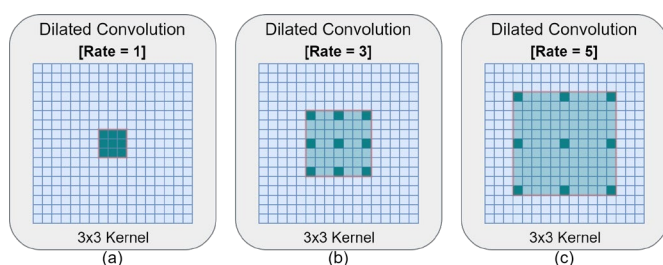**FIGURE 2. Network architecture of ChoroidNET.**

FIGURE 3. Representation of increasingly dilated convolutions with 3×3 kernel and their receptive fields for (a) rate = 1 (equivalent to standard convolution), (b) rate = 3, and (c) rate = 5.
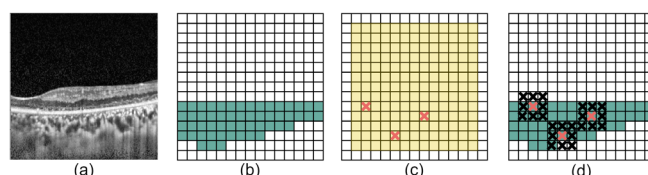

FIGURE 4. Illustration of how DropBlock drops features. (a) Input patch, (b) activation units (green area) of semantic information in (a) for the choroid layer, (c) DropBlock mask (yellow area) and sampled zero entries (red x's), and (d) zero entries on mask expanded to zero blocks (black x's around red x's).

IV. EXPERIMENTS

This section describes the datasets used in the experiment, existing state-of-the-art models used for comparison, and the experiment and its implementation details.

A. DATASETS

Kermany et al. [44] published a large OCT dataset that contains approximately 80,000 images. These images were acquired via spectral-domain OCT (SD-OCT; Spectralis, Heidelberg Engineering) and collected from the Shiley Eye Institute of the University of California San Diego, the California Retinal Research Foundation, Medical Center Ophthalmology Associates, Shanghai First People's Hospital, and the Beijing Tongren Eye Center. This dataset was constructed to evaluate methods for classifying OCT images into four categories, namely CNV, DME, Drusen, and Normal. Abnormalities, such as the neovascular

membrane and associated subretinal fluid in CNV images, retinal-thickening-associated intraretinal fluid in DME images, and multiple drusen, are present in their dataset. CNV and the appearance of drusen indicate clinical signs of AMD.

In the experiment, we evaluated the performance of ChoroidNET using 80 OCT images (20 images from each category) randomly selected from this OCT dataset. Figure 5 shows examples of OCT images used in our experiment. The ground truths of the choroid layer and choroidal vessels were annotated by an expert observer using the ibisPaint application [45].
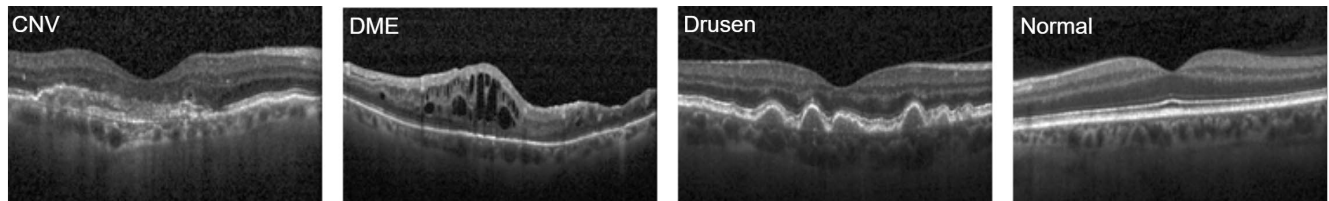

FIGURE 5. Examples of OCT images used in our experiment.

B. EXPERIMENT AND IMPLEMENTATION DETAILS

Ten images from each category were used to create a training set and the remaining images were used to create a test set. We enlarged the training set by using patches cropped from the original images (minimum dimensions: 230×495). Previous studies have shown that increasing the size of an image patch in a deep learning network provides a more precise segmentation performance since the network can capture more contextual information to make the prediction [46]. However, using a larger image patch requires larger memory. Under consideration of limited GPU memory, we chose a patch that is large enough to cover the choroid region and to be able to apply down-sampling operations in our network region, yet small enough to make the problem handleable. We randomly extracted 300 patches (dimensions: 224×224) from each image in a trainset set, for a total of 12,000 patches. Note that the areas of some patches overlapped. 90% of each training set was used for training and the remaining 10% was used for validation.

ChoroidNET was trained on each training set end-to-end using a computer with an Intel Core i7 CPU and an NVIDIA GeForce GTX 1070 Ti GPU. The training was performed for 50 epochs with a batch size of 4 and an initial learning rate of 0.0001. The RMSprop optimizer was used to adaptively reduce the learning rate. The loss function (L) was based on the sum of binary cross entropy loss (L_{BCE}) and Dice loss (L_D), as shown in Eqs. (2)-(4).

$$L(y, \hat{p}) = L_{BCE}(y, \hat{p}) + L_D(y, \hat{p}) \tag{2}$$

$$L_{BCE}(y, \hat{p}) = -(y \log(\hat{p}) + (1-y) \log(1-\hat{p})) \tag{3}$$

$$L_D(y, \hat{p}) = 1 - \frac{2y\hat{p}}{y + \hat{p}} \tag{4}$$

where $y \in [0,1]$ and $\hat{p} \in [0,1]$ respectively denote the set of pixels in the ground truth and the set of pixels predicted by the trained network.

The segmentation performance for the choroid layer and choroidal vessels was quantitatively evaluated in terms of five evaluation metrics, namely accuracy, the Dice coefficient, precision, recall, and specificity. The formulas for these metrics are shown in Table 2. The metrics were calculated based on four possibilities, namely true positive (TP), true negative (TN), false positive (FP), and false negative (FN). The numerical results are expressed as means ± standard deviation (SD).

TABLE 2. Formulas of evaluation metrics used in model comparison.

Metric	Formula
Accuracy	((TP+TN)/(TP+FP+TN+FN)) × 100
Dice coefficient	(2TP/(2TP+FP+FN)) × 100
Precision	(TP/(TP+FP)) × 100
Recall	(TP/(TP+FN)) × 100
Specificity	(TN/(TN+FP)) × 100

C. EXISTING METHODS

The performance of ChoroidNET is compared with that of U-Net++ L^3 [47], DRUNET [25], and Residual U-Net [31]. U-Net++ is an improved U-Net architecture based on nested and dense skip connections. U-Net++ was used to segment polyp, liver, and cell nuclei datasets. DRUNET and Residual U-Net adopt the structure of U-NET. DRUNET integrates residual blocks that comprise two dilated convolutions, instead of standard convolution blocks (except at the top level). DRUNET was designed for segmenting optic nerve head (ONH) tissues (including the choroid) in ONH-centered SD-OCT images. Residual U-Net inserts a residual connection between each pair of convolution blocks in its U-Net backbone. Residual U-Net is used for detecting the upper and lower boundaries of the choroid in foveal-centered SS-OCT images.

For a fair comparison, we trained and validated U-Net++, DRUNET, and Residual U-Net using the same training and

test sets used for ChoroidNET, and performed the same data augmentation, pre-processing, and DropBlock regularization as that in our experiment.

V. RESULTS

A. COMPARISON WITH EXISTING METHODS

This section presents the experimental results of the choroid layer and choroidal vessel segmentation.

The segmented images produced by U-NET++, DRUNET, Residual U-NET, and ChoroidNET were qualitatively compared with their corresponding ground truths and quantitatively evaluated. Figures 6 and 7 show examples of the choroid layer and choroidal vessel segmentation results. Table 3 compares the performance of the choroid layer and choroidal vessel segmentation for the tested networks.

In general, the choroid layer segmentation results for ChoroidNET are qualitatively comparable to the ground truths. ChoroidNET shows the best segmentation performance (accuracy: 98.5 ± 0.2, Dice coefficient: 95.1 ± 0.4, precision: 94.1 ± 1.6, recall: 96.1 ± 0.9, specificity:

99.0 ± 0.3). U-Net++ segmented the choroid layer as smooth as the ground truths, and also had the high Dice coefficient (94.0 ± 1.1) and recall (96.0 ± 0.8). However, it was slightly inferior to ChoroidNET in terms of all evaluation metrics and oversegmented areas outside the choroid layer for DME images. The DRUNET produced irregular choroid boundaries. Residual U-Net results are similar to the ground truths; however, the segmented boundaries of the choroid are not smooth.

ChoroidNET outperformed the other models in terms of choroidal vessel segmentation performance. It had the highest accuracy (97.7 ± 0.4), Dice coefficient (82.4 ± 2.4), and recall (87.2 ± 2.8). In particular, it had a significant improvement on recall by 6.2%, 4.0% and 4.7% compared to U-Net++, DRUNET, and Residual U-Net, respectively. U-Net++ had the highest precision (80.5 ± 5.7) and specificity (98.7 ± 0.3). Residual U-Net yielded the second-best performance in terms of the Dice coefficient (81.0 ± 2.3). For DME images, U-Net++ and Residual U-Net segmented irrelevant areas (intraretinal fluid) outside the choroid. DRUNET exhibited oversegmentation around the choroid upper layer in CNV and Drusen images.
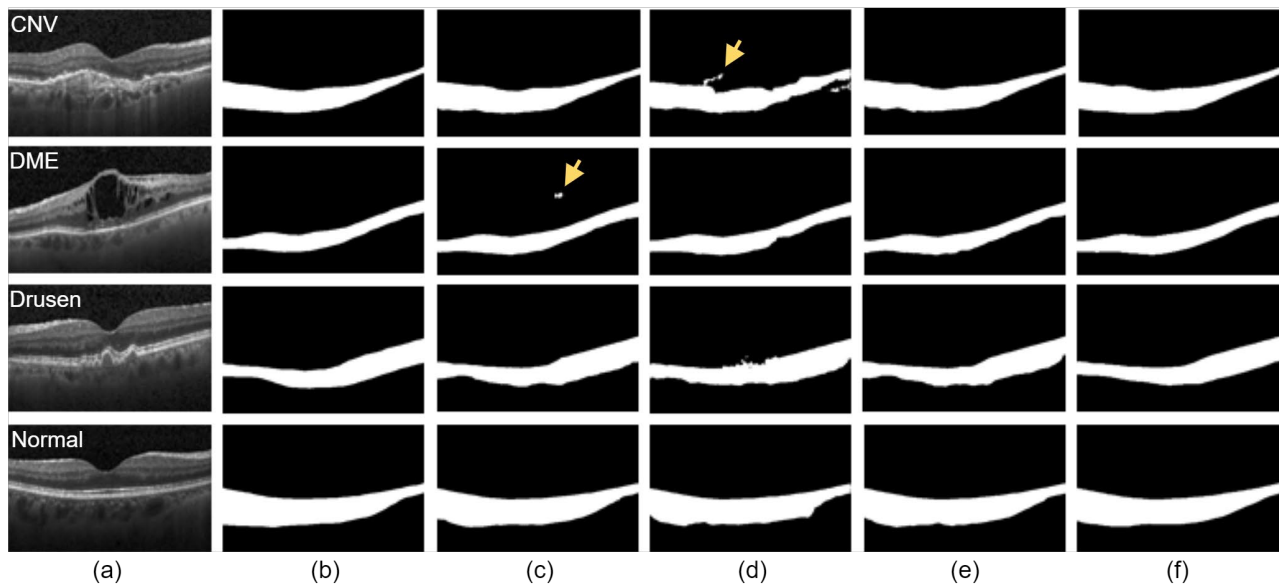

FIGURE 6. Choroid layer segmentation results. (a) Input, (b) ground truth, and results for (c) U-Net++, (d) DRUNET, (e) Residual U-Net, and (f) ChoroidNET. Yellow arrow indicates oversegmentation.

TABLE 3. Performance comparison of choroid layer and choroidal vessel segmentation (highest scores in bold).

|	Metric (mean ± SD)	U-Net++	DRUNET	Residual U-Net	ChoroidNET
Layer	Accuracy	98.2 ± 0.2	97.8 ± 0.1	98.1 ± 0.1	$\mathbf{98.5 \pm 0.2}$
	Dice coefficient	94.0 ± 1.1	92.5 ± 1.3	93.6 ± 1.0	$\mathbf{95.1 \pm 0.4}$
	Precision	92.2 ± 2.4	91.1 ± 2.7	92.9 ± 1.9	$\mathbf{94.1 \pm 1.6}$
	Recall	96.0 ± 0.8	94.0 ± 1.3	94.3 ± 0.8	$\mathbf{96.1 \pm 0.9}$
	Specificity	98.6 ± 0.3	98.4 ± 0.3	98.8 ± 0.2	$\mathbf{99.0 \pm 0.3}$
Vessels	Accuracy	97.6 ± 0.3	97.4 ± 0.4	97.6 ± 0.4	$\mathbf{97.7 \pm 0.4}$
	Dice coefficient	80.8 ± 2.0	80.0 ± 2.6	81.0 ± 2.3	$\mathbf{82.4 \pm 2.4}$
	Precision	$\mathbf{80.5 \pm 5.7}$	77.0 ± 5.3	79.5 ± 4.9	78.2 ± 5.6
	Recall	81.0 ± 2.2	83.2 ± 1.1	82.5 ± 1.5	$\mathbf{87.2 \pm 2.8}$
	Specificity	$\mathbf{98.7 \pm 0.3}$	97.6 ± 1.6	98.6 ± 0.3	98.4 ± 0.4
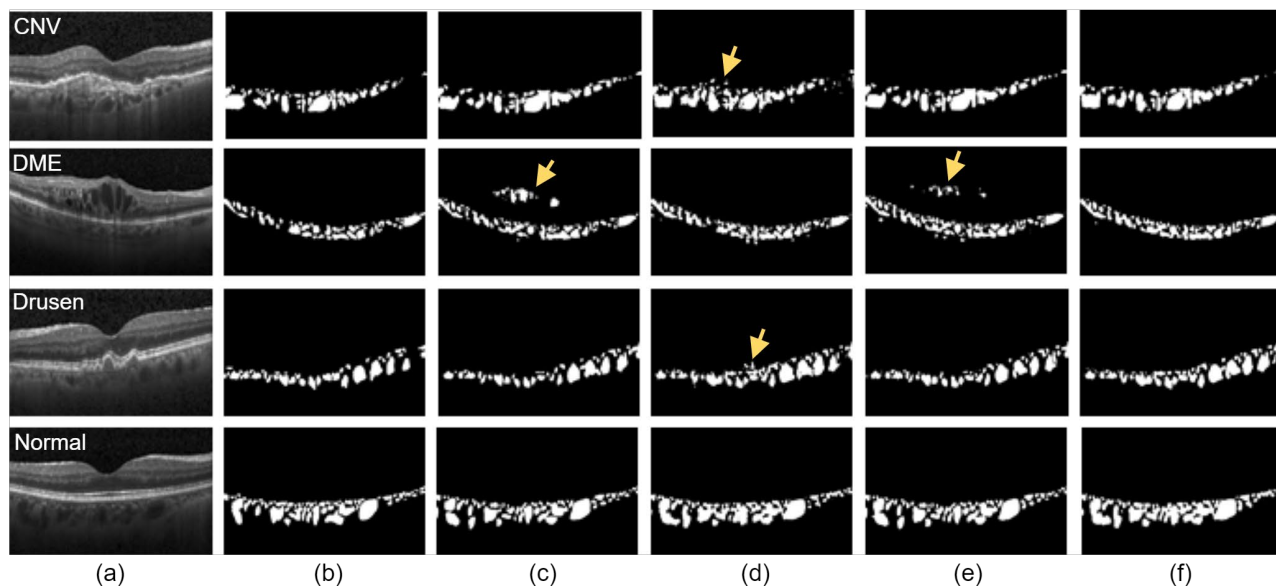
FIGURE 7. Choroidal vessel segmentation results. (a) Input, (b) ground truth, and results for (c) U-Net++, (d) DRUNET, (e) Residual U-Net, and (f) ChoroidNET. Yellow arrow indicates oversegmentation.

B. ABLATION STUDIES

To provide insight into each design element of ChoroidNET, we conducted four ablation studies. The ablation models were trained and validated using the same training and test sets. Figure 8 shows the architectures of the ablation models. Figures 9 and 10 show the segmentation results of the choroid layer and the choroidal vessels, respectively, for the ablation models and ChoroidNET. Table 4 compares the performance of ChoroidNET and its ablation models.

Ablation-1 and Ablation-2 did not use a dilation block in LSM. For choroid layer segmentation, the boundaries obtained by Ablation-1 and Ablation-2 are not as smooth as the ground truths. The choroid layer segmentation performance of Ablation-3 and Ablation-4 are the same as that of ChoroidNET. ChoroidNET outperforms Ablation-1 and Ablation-2 for the choroid layer segmentation and

shows an absolute improvement of 1.2% in terms of the Dice coefficient. The use of the dilation block in LSM improved the vessel segmentation results of Ablation-3 (81.5 ± 2.5), Ablation-4 (81.8 ± 2.5), and ChoroidNET (82.4 ± 2.4). This demonstrates the importance of the dilation block in LSM.

For choroid vessel segmentation, Ablation-1 had the highest recall (92.3 ± 2.2), but it oversegmented the region outside the choroid layer and thus had the lowest precision (68.6 ± 5.6). Ablation-2 slightly outperforms Ablation-1 by 0.6% in terms of the absolute Dice coefficient. This highlights the efficiency of the dilation block in VSM. The performance improvements (in terms of the Dice coefficient) of ChoroidNET over the four ablation models are 3.7%, 3.1%, 0.9%, and 0.6%, respectively. The improvement of ChoroidNET over Ablation-4 demonstrates the effectiveness of the connection between LSM and VSM.

TABLE 4. Performance comparison of ablation models and ChoroidNET.

|	Metric (mean ± SD)	Ablation-1	Ablation-2	Ablation-3	Ablation-4	ChoroidNET
Layer	Accuracy	98.2 ± 0.3	98.2 ± 0.3	98.5 ± 0.2	98.5 ± 0.2	98.5 ± 0.2
	Dice coefficient	93.9 ± 1.2	93.9 ± 1.2	**95.1 ± 0.4**	**95.1 ± 0.4**	**95.1 ± 0.4**
	Precision	92.6 ± 2.2	92.6 ± 2.2	94.1 ± 1.6	94.1 ± 1.6	94.1 ± 1.6
	Recall	95.1 ± 1.0	95.1 ± 1.0	96.1 ± 0.9	96.1 ± 0.9	96.1 ± 0.9
	Specificity	98.8 ± 0.3	98.8 ± 0.3	99.0 ± 0.3	99.0 ± 0.3	99.0 ± 0.3
Vessels	Accuracy	96.9 ± 0.4	97.1 ± 0.4	97.5 ± 0.4	97.5 ± 0.4	**97.7 ± 0.4**
	Dice coefficient	78.7 ± 3.2	79.3 ± 2.2	81.5 ± 2.5	81.8 ± 2.5	**82.4 ± 2.4**
	Precision	68.6 ± 5.6	72.6 ± 4.4	76.2 ± 5.3	76.5 ± 5.4	**78.2 ± 5.6**
	Recall	**92.3 ± 2.2**	87.5 ± 2.1	87.5 ± 2.1	87.7 ± 1.9	87.2 ± 2.8
	Specificity	97.2 ± 0.4	97.8 ± 0.2	98.2 ± 0.3	98.2 ± 0.4	**98.4 ± 0.4**
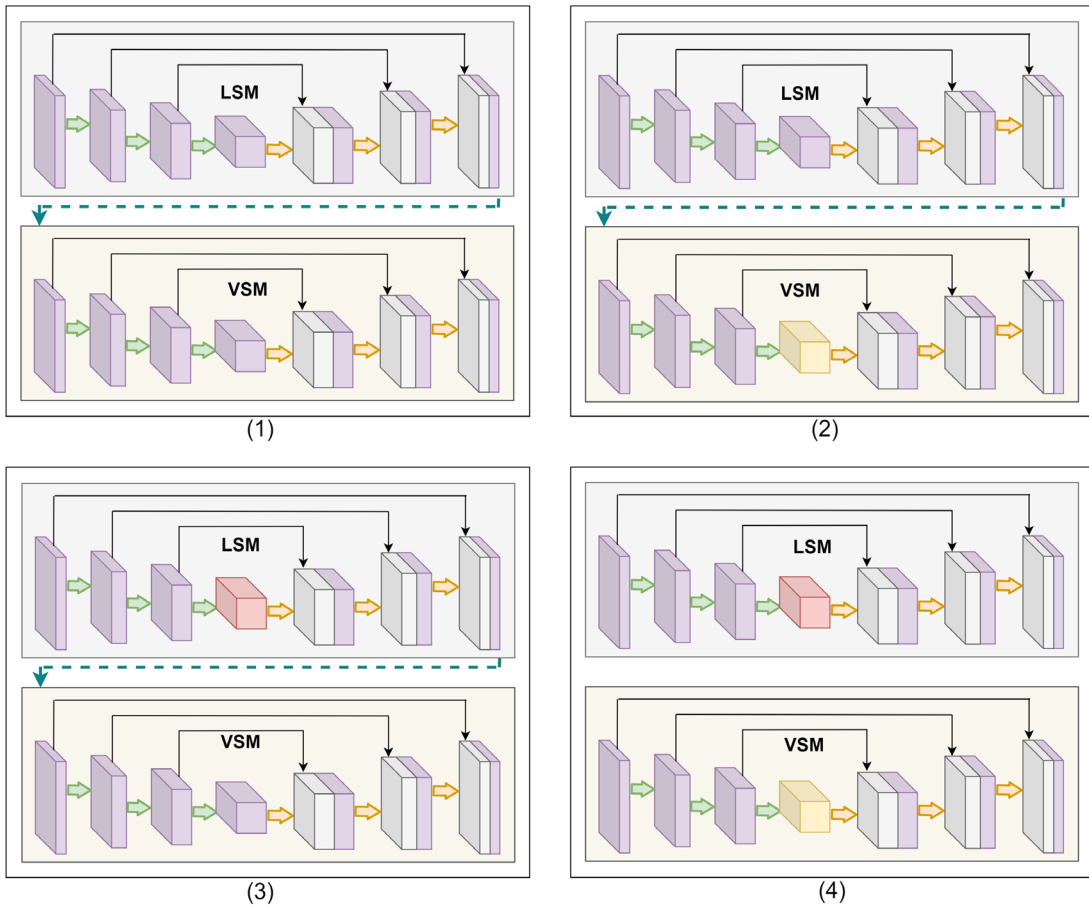
FIGURE 8. Ablation models of ChoroidNET (1) without dilation blocks in LSM and VSM, (2) without dilation block in LSM, (3) without dilation block in VSM, and (4) without connection between LSM and VSM.
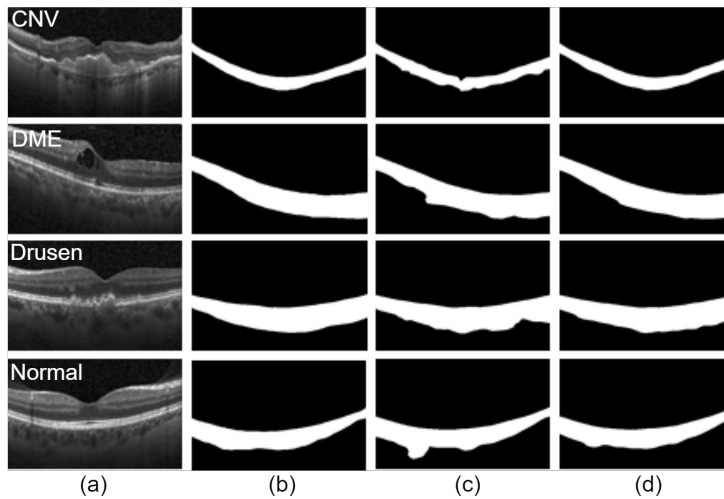

FIGURE 9. Choroid layer segmentation results. (a) Input, (b) ground truth, and results for (c) Ablation-1 and Ablation-2 and (d) Ablation-3, Ablation-4, and ChoroidNET.
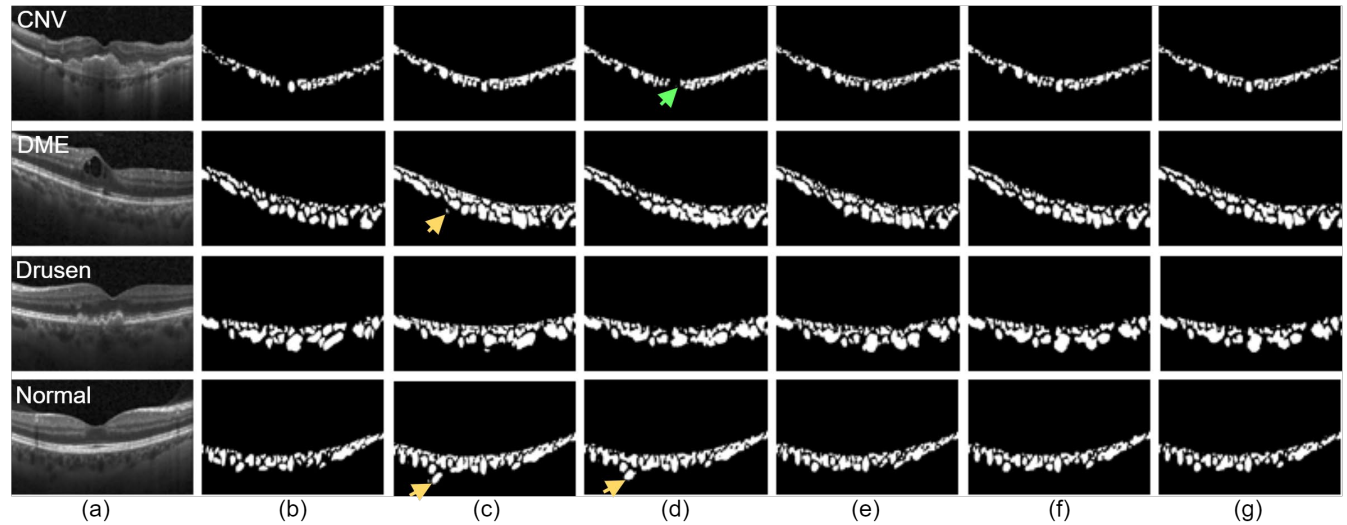
FIGURE 10. Choroidal vessel segmentation results. (a) Input, (b) ground truth, and results for (c) Ablation-1, (d) Ablation-2, (e) Ablation-3, (f) Ablation-4, and (g) ChoroidNET. Yellow and green arrows indicate over- and undersegmentation, respectively.

C. INTRA-OBSERVER VARIABILITY

For the assessment of intra-observer variability, our observer repeated annotating process for the choroid layer and choroidal vessels. Table 5 shows the variability between two sets of ground truths (GT1 and GT2) and ChoroidNET's segmentation. Intraclass correlation coefficient (ICC) was used to measure the variabilities. The ICC value of 1 indicates the highest agreement between the two observations. The intra-observer reproducibility of choroid layer and vessel segmentation between GT1 and GT2 were excellent (Dice coefficient: 96.1 ± 1.1 and 84.1 ± 2.6) and (ICC: 0.983, 0.971). ChoroidNET also produced a high agreement with GT1 and GT2, (Dice coefficient: 95.1 ± 0.4, 95.1 ± 2.8) for choroid layer segmentation and (Dice coefficient: 82.4 ± 2.4, 82.1 ± 2.8) for choroidal vessel segmentation. Figure 11 shows ChoroidNET's segmentation results and their corresponding ground truths.

D. CONSISTENCY OF THE PROPOSED NETWORK

We included 80 more images (20 images each from CNV, DME, Drusen, and Normal) for validating the consistency of our proposed network. The proposed model was trained on new training and test sets (40 images each). The training and validation processes were performed as same as the previous training. We then compared the performances of two distinct trained models using two test sets. Table 6 presents the quantitative performance of the proposed network for four sets. Set-1 corresponds to the results of test set-1 and the trained model-1, set-2 corresponds to results of test set-2 and the trained model-1, set 3 corresponds to results of test set-1 and the trained model-2, and set-4 corresponds to results of test set-2 and the trained model-2, respectively. Figure 12 shows examples of the choroid layer and choroidal vessel segmentation results of test set-2. The mean Dice coefficients of four sets were 95.1 ± 0.4, 95.7 ± 0.5, 93.5 ± 1.3, 96.4 ± 0.5 for choroid layer segmentation, and 82.4 ± 2.4, 84.3 ± 0.3, 82.2 ± 2.1, 85.1 ± 0.2 for choroidal vessel segmentation. Thus, ChoroidNET showed consistent and good performance on newly tested CNV, DME, Drusen, and Normal images.

TABLE 5. Performance difference of intra-observer variability.

|	Metric (mean ± SD)	GT1 vs GT2	GT1 vs ChoroidNET	GT2 vs ChoroidNET
Layer	Accuracy	98.8 ± 0.3	98.5 ± 0.2	98.5 ± 0.8
	Dice coefficient	96.1 ± 1.1	95.1 ± 0.4	95.1 ± 2.8
	Precision	97.3 ± 1.5	94.1 ± 1.6	95.0 ± 4.8
	Recall	95.0 ± 2.6	96.1 ± 0.9	95.3 ± 3.2
	Specificity	99.5 ± 0.4	99.0 ± 0.3	99.1 ± 0.8
	ICC	0.983	0.955	0.964
Vessels	Accuracy	98.0 ± 0.8	97.7 ± 0.4	97.6 ± 0.9
	Dice coefficient	84.1 ± 2.6	82.4 ± 2.4	82.1 ± 2.8
	Precision	84.4 ± 4.5	78.2 ± 5.6	88.2 ± 3.1
	Recall	83.8 ± 3.0	87.2 ± 2.8	76.7 ± 5.1
	Specificity	98.9 ± 0.5	98.4 ± 0.4	98.2 ± 0.8
	ICC	0.971	0.840	0.861
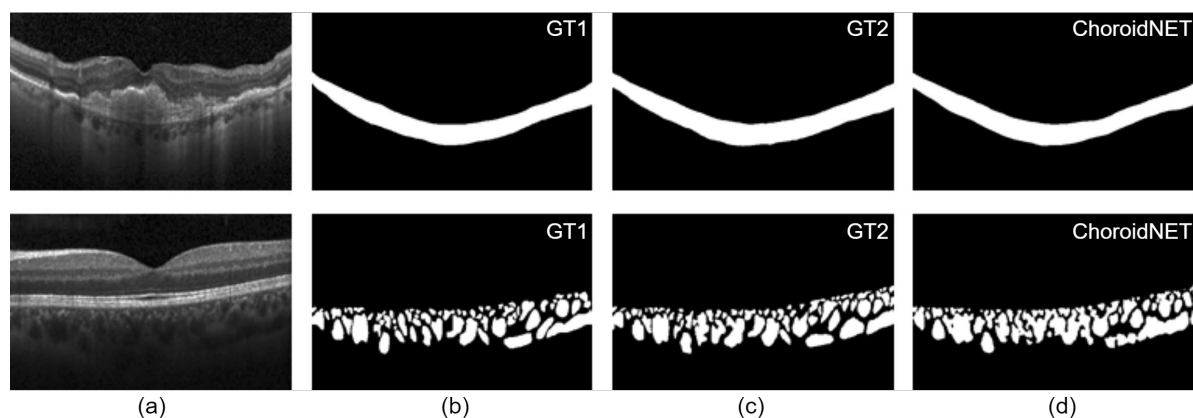
FIGURE 11. Intra-observer variability (a) Input, (b) ground truth (GT1), (c) ground truth (GT2), and (d) ChoroidNET result. (1st row – choroid layer and 2nd row – choroidal vessels)

TABLE 6. Quantitative performance of the proposed network for four sets.

|	Metric (mean ± SD)	Set-1	Set-2	Set-3	Set-4
Layer	Accuracy	98.5 ± 0.2	99.0 ± 0.1	98.0 ± 0.4	99.1 ± 0.2
	Dice coefficient	95.1 ± 0.4	95.7 ± 0.5	93.5 ± 1.3	96.4 ± 0.5
	Precision	94.1 ± 1.6	97.3 ± 0.3	89.8 ± 2.9	97.1 ± 0.8
	Recall	96.1 ± 0.9	94.1 ± 0.9	97.6 ± 0.8	95.7 ± 0.8
	Specificity	99.0 ± 0.3	99.6 ± 0.1	98.1 ± 0.5	99.6 ± 0.1
Vessels	Accuracy	97.7 ± 0.4	98.3 ± 0.2	97.7 ± 0.4	98.4 ± 0.2
	Dice coefficient	82.4 ± 2.4	84.3 ± 0.3	82.2 ± 2.1	85.1 ± 0.2
	Precision	78.2 ± 5.6	81.1 ± 1.9	79.2 ± 5.7	83.8 ± 1.2
	Recall	87.2 ± 2.8	87.8 ± 1.9	85.4 ± 3.7	86.5 ± 1.7
	Specificity	98.4 ± 0.4	98.9 ± 0.1	98.5 ± 0.4	99.1 ± 0.1
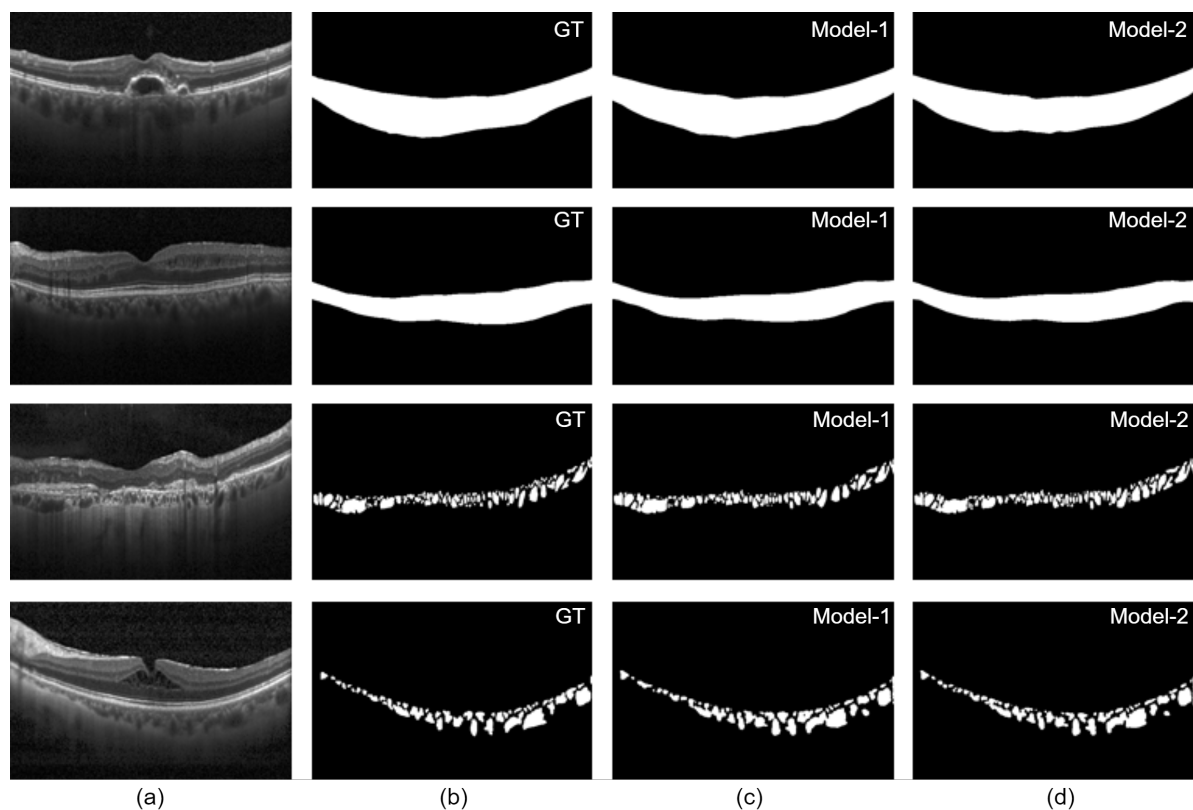
FIGURE 12. Choroid layer and vessel segmentation results of ChoroidNET using test set-2 (a) Input, (b) ground truth, (c) model-1, and (d) model-2. (1st row – choroid layer and 2nd row – choroidal vessels)

VI. DISCUSSION

We now present a qualitative and quantitative segmentation analysis of the choroid layer and choroidal vessels. The experimental results in Table 3 confirm that ChoroidNET is the best state-of-the-art model for the segmentation of the choroid layer and choroidal vessels.

In an eye with DME, an accumulation of fluid with cystic properties usually occurs in the retinal layers. In an OCT image, those accumulated fluid regions are similar to the characteristics of choroidal vessels. For DME images, U-Net++ and Residual U-Net had inconsistent vessel segmentation performance compared to that of DRUNET and ChoroidNET, as shown with the yellow arrows in Figure 7 (c and e). The objective of the standard convolutions in U-Net++ and Residual U-Net is to extract the spatial information in the image. A deeper network can learn more semantic information. However, spatial information is lost at deeper layers, and thus the network predicts incorrect regions outside the choroid layer. Dilated convolutions reduce the loss of spatial information by expanding the receptive field of the network. Thus, the dilated convolutions in DRUNET and ChoroidNET facilitate the creation of large-scale feature maps with rich spatial information. The segmentation performance of DRUNET and ChoroidNET is thus more consistent for DME images.

In the U-Net architecture, the number of filters is doubled after down-sampling in the encoder path and halved after up-sampling in the decoder path. However, in the DRUNET architecture, only 16 filters are used in both standard blocks and residual blocks. DRUNET thus had poor vessel segmentation performance for CNV and Drusen images. The filter of a convolutional layer captures the patterns in image data. A higher number of filters allows the network to learn more complex patterns (abstractions) contained in image data and extract useful features. As a result, DRUNET was unable to separate the choroid pattern from the neovascular membrane in CNV images and mistakenly segment small drusen (which occurs in the complex between RPE and the choroid) as the choroidal vessels, as illustrated with the yellow arrows in Figure 7 (d). U-Net++, Residual U-Net and ChoroidNET use a high number of filters (the same as that in U-Net), which considerably improves the recognition and segmentation of the choroid layer and vessels.

Overall, the segmentation performance of ChoroidNET is similar and consistent with the ground truths. U-Net++, DRUNET, and Residual U-Net are sensitive to the pathologies (subretinal and intraretinal fluid) present in CNV, DME, and Drusen images. In contrast, there is no significant difference in the segmentation performance of ChoroidNET for CNV, DME, Drusen, and Normal images.

The number of parameters used by a network depends on the number of filters. ChoroidNET and Residual U-Net each use approximately 4.5 million parameters (compared to 2.2 million for U-Net++ and only 40,000 for DRUNET) and thus

have a much higher computational cost and use much more memory. This is a major drawback of ChoroidNET.

We also evaluated the segmentation performance of ChoroidNET based on the prediction scores of the receiver operator characteristics area under the curve (ROC-AUC) and the precision-recall area under the curve (PR-AUC). ROC-AUC indicates the tradeoff between the true positive rate (TPR) and false positive rate (FPR). PR-AUC represents the tradeoff between precision and recall. The range of scores is [0, 1]. A higher score indicates a better model performance. ChoroidNET obtained (ROC-AUC: 0.997 ± 0.001, PR-AUC: 0.989 ± 0.002) for choroid layer segmentation and (ROC-AUC: 0.992 ± 0.001, PR-AUC: 0.906 ± 0.018) for choroidal vessel segmentation, respectively.

Further, we performed ablation studies to demystify the architecture of the proposed network. We also measured the intra-observer variability for choroid layer and vessel segmentation. To access the consistency and robustness of the proposed model, we tested ChoroidNET's performance using an additional dataset that contains 80 images (with CNV, DME, Drusen, and Normal).

In summary, ChoroidNET significantly outperforms U-Net++, DRUNET and Residual U-Net and is robust for images with various retinal pathologies. In addition, it provides good tradeoffs between TPR and FPR, and between precision and recall for both choroid layer and choroidal vessel segmentation. ChoroidNET is thus the most robust model.

VII. CONCLUSION

In this study, we proposed ChoroidNET, a robust segmentation model for segmenting both the choroid layer and choroidal vessels in OCT images. ChoroidNET uses U-NET as a backbone and adds dense dilated convolutions at the bottleneck of LSM and VSM. The performance of ChoroidNET was evaluated using an OCT dataset. The numerical results indicate that ChoroidNET outperforms U-Net++, DRUNET, and Residual U-Net, and is robust to cases of pathological abnormality (i.e., neovascular membrane and associated subretinal fluid in CNV, retinal-thickening-associated intraretinal fluid in DME, and multiple drusen).

Clinical research has shown that choroidal structures, in terms of changes in the luminal and stromal areas, and visual functions are highly correlated in diseased eyes [48-50]. Based on the segmentation results of ChoroidNET, our work could be extended to offer accurate quantification of clinical parameters derived from the choroid. These parameters can be used to find clinical correlations between choroidal changes and other clinical measures. It would be helpful for ophthalmologists to monitor changes in the choroid layer over time for various eye diseases.

In this work, we considered the segmentation of the choroid layer and choroidal vessels in OCT images. We

will consider the segmentation of the retinal layers, the RPE, and the sclera in future studies because the pathologies of other tissues in the retina are important for diagnosing diseases such as Alzheimer's disease [51], AMD, diabetic retinopathy, and scleritis.

ACKNOWLEDGMENT

REFERENCES

[1] S. R. Singh, K. K. Vupparabonia, A. Goud, B. Sopt, K. K. Dansingari, and J. Chhablani, "Choroidal imaging biomarkers," *Survey of Ophthalmology*, vol. 64, pp. 312–333, 2019.

[2] G. Yiu, S. J. Chiu, P. A. Petrou, E. Y. Chew, W. T. Wong, and C. A. Toth, "Relationship of central choroidal thickness with age-related macular degeneration status," *American Journal of Ophthalmology*, vol. 159, no. 4, pp. 617–626, 2015.

[3] A. Invernizzi, E. Benatti, M. Cozzi, S. Erba, S. Vaishnavi, K. K. Vupparaboina, G. Staurenghi, J. Chhablani, M. Gillies, and F. Viola, "Choroidal structural changes correlate with neovascular activity in neovascular age-related macular degeneration," *Investigative ophthalmology & visual science (iovs)*, vol. 59(10), pp. 3836–3841, 2018.

[4] R. Nourinia, H. Ahmadieh, E. Nekoei, P. Malekifar, and Z. Tofighi, "Changes in central choroidal thickness after treatment of diabetic macular edema with intravitreal bevacizumab correlation with central macular thickness and best correlated visual acuity," *Retina*, vol. 38, no. 5, pp. 970–97, 2018.

[5] D. S. Dhoot, S. Huo, A. Yuan, D. Xu, S. Srivistava, J. P. Ehlers, E. Traboulsi, and P. K. Kaiser, "Evaluation of choroidal thickness in retinitis pigmentosa using enhanced depth imaging optical coherence tomography," *British Journal of Ophthalmology*, vol. 99, pp. 66–69, 2013.

[6] R. Tan, R. Agrawal, S. Taduru, A. Gupta, K. Vupparabonia, and J. Chhablani, "Choroidal vascularity index in retinitis pigmentosa: An OCT study," *Ophthalmic Surgery, Lasers and Imaging Retina*, vol. 49, pp. 191–197, 2018.

[7] I.Y. Wong, H. Koizumi, and W.W. Lai, "Enhanced depth imaging optical coherence tomography," *Ophthalmic Surgery, Lasers and Imaging*, vol. 42, pp. 75–84, 2011.

[8] A. Y. Alibhai, C. Or, and A. J. Witkin, "Swept source optical coherence tomography: A review," *Current Ophthalmology Reports*, vol. 6, pp. 7–16, 2018.

[9] O. Ronneberger, P. Fischer, and T. Brox, "U-net: Convlutional networks for biomedical image segmentation," in *International Conference on Medical Image Computing and Computer-Assisted Intervention (MICCAI)*, pp. 234–241, 2015.

[10] Z. Hu, X. Wu, Y. Ouyang, Y. Ouyang, and S. R. Sadda, "Semiautomated segmentation of the choroid in spectral-domain optical coherence tomography volume scans," *Investigative ophthalmology & visual science (iovs)*, vol. 54, pp. 1722–1729, 2013.

[11] H. Danesh, R. Kafieh, H. Rabbani, and F. Hajizadeh, "Segmentation of choroidal boundary in enhanced depth imaging OCTs using a multiresolution texture-based modeling in graph cuts," *Computational and Mathematical Methods in Medicine*, vol, 2014, 479268, 2014.

[12] S. Masood, B. Sheng, P. Li, R. Shen, R. Fang, and Q. Wu, "Automatic choroid layer segmentation using normalized graph cut," *The Institution of Engineering and Technology (IET)*, vol. 4, no. 3, pp. 397–411, 2017.

[13] Q. Chen, W. Fan, S. Niu, J. Shi, H. Shen, and S, Yuan, "Automated choroid segmentation based on gradual intensity distance in HD-OCT images, *Optics Express*, vol. 23, no. 7, pp. 8974–8994, 2015.

[14] J. Tian, P. Marziliano, M. Baskaran, T. A. Tun, and T. Aung, "Automatic segmentation of the choroid in enhanced depth imaging optical coherence tomography images," *Biomedical Optics Express*, vol. 9, no. 7, pp. 3049–3065, 2013.

[15] M. A. Hussian, A. Bhuiyan, H. Ishikawa, R. T. Smith, J. S. Schuman, and R. Kotagiti, "An automated method for choroidal thickness measurement from enhanced depth imaging optical coherence tomography images," *Computerized Medical Imaging and Graphics*, vol. 63, pp. 41–51, 2018.

[16] B. Salafian, R. Kafieh, A. Rashno, M. Pourazizi, and S. Sadri, "Automatic segmentation of choroid layer in EDI OCT images using graph theory in neutrosophic space," *arXiv: Image and Video Processing*, 2018.

[17] H. Lu, N. Boonarpha, M. T. Kwong, and Y. Zheng, "Automated segmentation of the choroid in retinal optical coherence tomography images," *35th Annual International Conference of the IEEE EMBS*, pp. 5869–5872, 2013.

[18] C. Wang, Y. X. Wang, and Y. Li, "Automatic choroid layer segmentation using markov random field and level set method." *IEEE Journal of Biomedical and Health Informatics*, vol. 21, no. 6, pp. 1694–1702, 2017.

[19] X. Sui, Y. Zheng, B. Wei, H. Bi, J. Wu, X. Pan, Y. Yin, and S. Zhang, "Choroid segmentation from optical coherence tomography with graph-edge weights learned from deep convolutional neural networks," *Neurocomputing*, 237, pp. 332–341, 2017.

[20] S. Masood, R. Fang, P. Li, H. Li, B. Sheng, A. Mathavan, X. Wang, P. Yang, Q. Wu, J. Qin, and W. Jia, "Automatic choroid layer segmentation from optical coherence tomography images using deep learning," *Scientific Reports*, vol. 9:3058, 2019.

[21] J. Kugelman, D. Alonso-Caneiro, S. A. Read, J. Hamwood, S. J. Vincent, F. K. Chen, and M. J. Collins, "Automatic choroidal segmentation in OCT images using supervised deep learning methods, *Scientific Reports*, vol. 9, 13298 (2019).

[22] D. Alonso-Caneiro, J. Kugelman, J. Hamwood, S. A. Read, S. J. Vincent, F. K. Chen, and M. J. Collins, "Automatic retinal and choroidal boundary segmentation in OCT images using patch-based supervised machine learning methods," *Asian Conference on Computer Vision (ACCV)*, pp. 215–228, 2019.

[23] M. Chen, J. Wang, I. Oguz, B. L. VanderBeek, and J. C. Gee, "Automated segmentation of the choroid in EDI-OCT images with retinal pathology using convolutional neural networks," *Fetal, Infant and Ophthalmic Medical Image Analysis (OMIA)*, pp. 177–184, 10554 (2017).

[24] V. Badrinarayanan, A. Kendall, and R. Cipolla, "SegNet: A deep convolutional encoder-decoder architecture for image segmentation," *IEEE Transactions on Pattern Analysis and Machine Intelligence*, vol. 12, no. 12, pp. 2481–2495, 2017.

[25] S. K. Devalla, P. K. Renukanand, B. K. Sreedhar, G. Subramanian, L. Zhang, S. Perera, J. Mari, K. S. Chin, T. A. Tun, N. G. Strouthidis, T. Aung, A. H. Thiery, and M. J. A. Girard, "DRUNET: a dilated-residual U-Net deep learning network to segment optic nerve head tissues in optical coherence tomography images," *Biomedical Optics Express*, vol. 9, no. 7, pp. 3244–3264, 2018.

[26] H. Zhang, J. Yang, K. Zhou, F. Li, Y. Hu, Y. Zhao, C. Zheng, X. Zhang, and J. Liu, "Automatic segmentation and visualization of choroid in OCT with knowledge infused deep learning." *IEEE Journal of Biomedical and Health Informatics*, vol. 24, no. 12, pp. 3408–3420, 2020.

[27] W. P. Hsia, S. L. Tse, C. J. Chang, and Y. L. Huang, "Automatic segmentation of choroid layer using deep learning on spectral domain optical coherence tomography," *Applied Sciences*, vol. 11, 5488, 2021.

[28] N. Srinath, A. Patil, V. K. Kumar, S. Jana, J. Chhablani, and A. Richhariya, "Automated detection of choroid boundary and vessels in optical coherence tomography images," in *Engineering in Medicine and Biology Society (EMBC), 2014 36th Annual International Conference of the IEEE*, pp. 166–169, 2014.

[29] X. Liu, L. Bi, Y. Xu, D. Feng, J. Kim, and X. Xu, "Robust deep learning method for choroidal vessel segmentation on swept source optical coherence tomography images," *Biomedical Optics Express*, vol. 10, no. 4, pp. 1601–1612, 2019.

[30] G. Lin, A. Milan, C. Shen, and I. Reid, "RefineNet: Multi-path refinement networks for high-resolution semantic segmentation," in *2017 IEEE Conference on Computer Vision and Pattern Recognition (CVPR)*, pp. 5168–5177, 2017.

This article has been accepted for publication in a future issue of this journal, but has not been fully edited. Content may change prior to final publication. Citation information: DOI 10.1109/ACCESS.2021.3124993, IEEE Access

Author Name: Preparation of Papers for IEEE Access (September 2021)

[31] G. Zheng, Y. Jiang, C. Shi, H. Miao, X. Yu, Y. Wang, S. Chen, Z. Lin, W. Wang, F. Lu, and M. Shen, "Deep learning algorithms to segment and quantify the choroidal thickness and vasculature in swept-source optical coherence tomography images," *Journal of Innovative Optical Health Sciences*, vol. 14, no. 1 (2140002), 2021.

[32] Z. Zhang, Q. Liu, and Y. Wang, "Road extraction by deep residual U-Net," *IEEE Geoscience and Remote Sensing Letters*, vol. 15, pp. 749–753, 2018.

[33] H. Zhou, Z. Chu, Q. Zhang, Y. Dai, G. Gregori, P. J. Rosenfeld, and R. K. Wang, "Attenuation correction assisted automatic segmentation for assessing choroidal thickness and vasculature with swept-source OCT," *Biomedical Optics Express*, vol. 9, no. 12, pp. 6067–6080, 2018.

[34] Z. Al-Ameen, G. Sulong, A. Rehman, A. Al-Dhelaan, T. Saba, and M. Al-Rodhaan, "An innovative technique for contrast enhancement of computed tomography images using normalized gamma-corrected contrast-limited adaptive histogram equalization," *EURASIP Journal on Advances in Signal Processing*, 2015:32, 2015.

[35] G. Ghiasi, T. Lin, and Q. V. Le, "DropBlock: A regularization method for convolutional networks," In: *Conference of Neural Information and Processing Systems, NeurIPS*, 2018.

[36] S. Ioffe and C. Szegedy, "Batch normalization: accelerating deep network training by reducing internal covariate shift," in *Proceedings of the 32nd International Conference on Machine Learning*, vol. 37 (JMLR.org, Lille, France, 2015), pp. 448–456, 2015.

[37] A. F. Agarap, "Deep learning using rectified linear units (RELU)," *Neural and Evolutionary Computing*, arXiv:1803.08375 [cs.NE], 2018.

[38] M. Drozdzal, E. Vorontsov, G. Chartrand, S. Kadoury, and C.Pal, "The importance of skip connections in biomedical image segmentation," *Deep Learning and Data Labeling for Medical Applications*, pp. 179–187, 2016.

[39] F. Yu, and V. Koltun, "Multi-scale context aggregation by dilated convolutions," in *International Conference on Learning Representations, ICLR*, 2016.

[40] L. Chen, G. Papandreou, I. Kokkinos, K. Murphy, and A. L.Yuille, "DeepLab: Semantic image segmentation with deep convolutional nets, atrous convolution, and fully connected CRFs," *IEEE Transactions on Pattern Analysis and Machine Intelligence*, vol. 40, no. 4, pp. 834–848, 2018.

[41] R. Hamaguchi, A. Fujita, K. Nemoto, T. Imaizumi, and S. Hikosaka, "Effective use of dilated convolutions for segmenting small object instances in remote sensing imagery," *2018 IEEE Winter Conference on Applications of Computer Vision*, vol. 1, pp. 1442–1450, 2018.

[42] N. Srivastava, G. Hinton, A. Krizhevsky, I. Sutskever, and R. Salakhutdinov, "Dropout: a simple way to prevent neural networks from overfitting," *Journal of Machine Learning Research*, vol. 15, pp. 1929–1958, 2014.

[43] G. Ghiasi, T. Lin, R. Pang, and Q. V. Le, "NAS-FPN: Learning scalable feature pyramid architecture for object detection," in *IEEE Conference on Computer Vision and Pattern Recognition, CVPR*, 2019.

[44] D. Kermany, K. Zhang, M. Goldbaum et al., "Indentifying medical diagnosis and treatable diseases by image-based deep learning," *Cell*, vol. 172, no. 5, pp. 1122–1131, 2018.

[45] ibisPaint Application, https://ibispaint.com, last accessed 2021/07/28.

[46] J. Hamwood, D. Alonso-Caneiro, S. A. Read, S. J. Vincent, and M. J. Collins, "Effect of patch size and network architecture on a convolutional neural network approach for automatic segmentation of OCT retinal layers," *Biomedical Optics Express*, vol. 9, no. 7, pp. 3049–3065, 2018.

[47] Z. Zhou, Md. M. R. Siddiquee, N. Tajbakhsh, and J. Liang, "U-Net++: A nested architecture for medical image segmentation," *Computer Vision and Pattern Recognition*, arXiv:1807.10165 [cs.CV], 2018.

[48] G. Liu, X. Liu, H. Li, Q. Du, and F. Wang, "Optical coherence tomography analysis of retina in retinitis pigmentosa patients," *Ophthalmic Research*, vol. 56, pp. 111–122, 2016.

[49] M. Egawa, Y. Mitamura, M. Niki, H. Sano, G. Miura, A. Chiba, S. Yamamoto, S. Sonoda, and T. Sakamoto, "Correlations between choroidal structures and visual functions in eyes with retinitis pigmentosa." *Retina, Journal of Retinal and Vitreous Diseases*, vol. 39, no. 12, pp. 2399–2409, 2019.

[50] K. Okawa, T. Inoue, R. Asaoka et al., "Correlation between choroidal structure and smoking in eyes with central serous chorioretinopathy," *PLoS ONE*, vol. 16, no. 3, e029073, 2021.

[51] J. den Haan, L. Csinscik, T. Parker, et al., "Retinal thickness as potential biomarker in posterior cortical atrophy and typical Alzheimer's disease," *Alzheimer's Research & Therapy*, vol. 11:62, 2019.

TIN TIN KHAING received her M.S. in Engineering and Technology from Thammasat University, Thailand, in 2017. She is currently pursuing double doctoral degrees from Chiba University, Japan, and Thammasat University. Her current research interests include medical image processing, disease-specific analysis of retinal images, and their potential applications.

TAKAYUKI OKAMOTO received his M.E. degree from Chiba University in 2017. He is currently pursuing the Ph.D. degree in Graduate School of Science and Engineering, Chiba University. His current research interests include medical image processing, image reconstruction and machine learning.

CHEN YE (Member, IEEE) received the B.E. degree in software engineering from Dalian Maritime University, Dalian, China, in 2012, the M.E. degree in electronics and information systems from Akita Prefectural University, Yurihonjo, Japan, in 2017, and the Ph.D. degree from Center for Information and Computer Science, Keio University, Yokohama, Japan, in 2019. He was a Project Research Associate (Research) with the Faculty of Science and Technology, Keio University, from 2019 to 2021. He is currently a Specially Appointed Assistant Professor with the Center for Frontier Medical Engineering, Chiba University. Concurrently, he is also a Visiting Assistant Professor, Keio University. He received the IEEE Student Awards Encouragement Prize (Sendai Section) in 2015 and the Telecom System Technology Student Award (Telecommunications Advancement Foundation) in 2018. He is a member of IEEE, and a member of the Institute of Electronics, Information and Communication Engineers (IEICE).

MD. ABDUL MANNAN received the B.Sc. and M.Sc. degree in Applied Physics and Electronics from the University of Rajshahi, Bangladesh in 1999 and 2001, respectively. He also received the Ph.D. degree in 2012 from the Saitama University. After working with Osaka University, Equos Research and Chiba University, he joined the Seikei University as a researcher. His research interests are mainly in computer vision and pattern recognition.

HIROTAKA YOKOUCHI received his M.D. and Ph.D. degrees from Graduate School of Medicine, Chiba University in 2001 and 2007, respectively. Since 2011, he has worked as an ophthalmologist at Department of Ophthalmology, Chiba University Hospital. Currently, he is an associate professor at Department of Ophthalmology, Chiba University Hospital, and specializes in neuro-ophthalmology. His current research interests include image

15

This article has been accepted for publication in a future issue of this journal, but has not been fully edited. Content may change prior to final publication. Citation information: DOI 10.1109/ACCESS.2021.3124993, IEEE Access

IEEE *Access*

Author Name: Preparation of Papers for IEEE Access (September 2021)

analysis of ocular diseases, particularly the analysis of the close relationship between optical coherence tomography (OCT) images and ocular diseases.

KAZUYA NAKANO received his M.S. and Ph.D. degrees from Tokyo Institute of Technology in 2007 and 2013, respectively. Since 2019, he has been an assistant professor at the Institute for Tenure Track Promotion, University of Miyazaki. He worked for Mizuho Information & Research Institute (MHIR) from 2007 to 2009. He was an assistant professor in Nippon Sport Science University from 2013 to 2014 and Tokyo University of Science from 2015 to 2016. He was a specially appointed assistant professor in the Center for Frontier Medical Engineering, Chiba University from 2017 to 2019. His current research interests include optical security, information photonics, and biomedical optics.

PAKINEE AIMMANEE is an Associate Professor at Thammasat University. She received her B.S. in Mathematics from the University of Delaware, USA, and her M.S. and Ph.D. in Applied Mathematics from the University of Colorado, USA. She joined Thammasat University, Thailand in 2005. Her research interests include medical image processing and audio processing.

STANISLAV S. MAKHANOV is a Full Professor and a Head of Center of Excellence in Biomedical Engineering of Thammasat University, Thailand. His M.S. and Ph.D. degrees are in Applied Mathematics from Moscow State University and the Computing Center of the Russian Academy of Science. His research areas are medical image processing, robotics, pattern recognition and grid generation.

HIDEAKI HANEISHI is a Full Professor of the Center for Frontier Medical Engineering (CFME) and also a Director of CFME. He received his M.S. degree in 1987 and Ph.D. in 1990 from the Tokyo Institute of Technology. He joined Chiba University as a Research Associate, in 1990. He was a Visiting Research Scientist with the Department of Radiology, University of Arizona, from 1995 to 1996.